Factorial Design of Experiments for Optimization of Photocatalytic Degradation of Tartrazine by Zinc Oxide (ZnO) Nanorods with Different Aspect Ratios

Andrew W. Skinner[1,2], Anthony M. DiBernardo[1,3], Arvid M. Masud[4],

Nirupam Aich[4], Alexandre H. Pinto[1,5*]

1 - Department of Chemistry, Ithaca College, 953 Danby Road, Ithaca, NY, 14850, USA

2 – Pacific Northwest National Laboratory, 902 Battelle Boulevard, Richland, WA, 99352, USA

3 – Department of Chemistry, University of Wisconsin Madison, 1101 University Avenue Madison, WI, 53706, USA

4 - Department of Civil, Structural and Environmental Engineering, University at Buffalo, The State University of New York, 232 Jarvis Hall, Buffalo, NY, 14260, USA

5 – Department of Chemistry & Biochemistry, Manhattan College, 4513 Manhattan College Parkway, Riverdale, NY 10471, USA
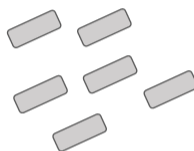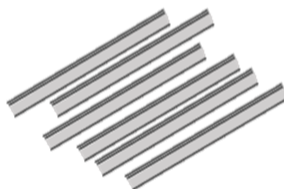
* alex.pinto@manhattan.edu
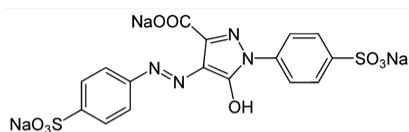
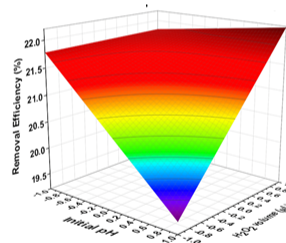**Tartrazine**

Photocatalytic Degradation by ZnO Nanorods

ZnO Low Aspect Ratio

ZnO High Aspect Ratio

2^4 Factorial Design

Abstract

The photocatalytic degradation of the azo dye tartrazine using zinc oxide (ZnO) as photocatalyst under ultraviolet light was investigated using a 2^4 factorial design. The variables studied were the aspect ratio of ZnO nanorods, the ZnO load, the initial pH of tartrazine solution, and the H_2O_2 volume. These variables were studied aiming to maximize the tartrazine removal efficiency and the pseudo-1st-order rate constant of the removal process. The ZnO aspect ratio was tuned by varying the Lewis base during the synthesis, hexamethylenetetramine (HMTA) was used to prepare ZnO with low aspect ratio (ZnO_LowAR), and NaOH was used to prepare ZnO with high aspect ratio (ZnO_HighAR). The microstructural characterizations indicated that ZnO_LowAR and ZnO_HighAR nanorods have similar structural, textural and optical properties. The only exception was the dimensions of the nanorods obtained, which could result in differences in the facets exposed on each type of nanorod surface. The factorial design revealed that ZnO aspect ratio, the initial pH of tartrazine solution, and the H_2O_2 volume all have primary significant effects, whereas the ZnO load is not significant neither in the tartrazine removal efficiency nor in the pseudo-1st-order rate constant. Statistical models considering the coefficients of the significant interactions were obtained, leading to reasonable predicted results in comparison to the results experimentally obtained. The conditions leading to highest removal efficiency (~92%) and pseudo-1st-order rate constant (3.81×10^{-2} min^{-1}) were carried out with ZnO_HighAR, initial pH 7, and without H_2O_2, which outperformed the TiO_2 P-25 under the same conditions.

1. Introduction

Water scarcity is a worldwide issue that demands attention. Some studies show that about two thirds of global population live under severe water scarcity condition, for at least a month during an year[1]. An important factor contributing to water scarcity is the water pollution. About 30% of accessible freshwater is used in industrial and urban settings, producing a large amount of wastewater containing diverse categories of chemicals in different concentrations[4]. A class of major water contaminants is the synthetic dyes.

It is estimated that about 10,000 tons of synthetic dyes are produced yearly, from that, 1-2% are discharged during the production, whereas about 1-10% are discharged due to use.[5] Among the many different chemical categories of dyes, azo dyes are the ones produced in largest amount, either by number or volume, comprising 70% of all the synthetic organic dyes produced worldwide[6]. Tartrazine (FD&C Yellow 5, C. I. Acid Yellow 23) is an yellow azo dye used in beverages, bakery products, and candies[7]. It is related to side effects like hyperactivity, asthma, migraines, eczema, thyroid cancer and lupus[8]. In this sense, it is necessary to search for efficient and sustainable methods to remove tartrazine from wastewater.

Photocatalysis is a type of advanced oxidation process (AOP) used to degrade water pollutant molecules in an efficient and straightforward way. Besides being a generally cost-effective process[9]. When semiconductors absorb electromagnetic radiation with energy equal or higher than its band gap, electrons are promoted from the valence to the conduction band, leaving positive holes in the valence band. The holes have enough potential to trigger additional interfacial reactions producing hydroxyl radicals (OH$^{\bullet}$), these radicals can oxidize, and consequently, degrade the organic pollutant molecules. Additionally, the electrons in the conduction band can be

transferred to oxygen producing O_2^-, which further can lead to production of H_2O_2, $OH^{\bullet}$, and aid in the degradation of the organic pollutant molecule[10,11].

Zinc oxide (ZnO) is a group II-VI semiconductor, with direct band gap of 3.37 eV, used as photocatalyst for degradation of several organic pollutant molecules, such as pharmaceutical molecules, like paracetamol[12] and amoxicillin[13]; textile and food dyes, like methylene blue and eosin Y[14]; and pesticides, like azoxystrobin and hexaconazole[15]. Other interesting ZnO features are its high thermal and mechanical stability at room temperature. Additionally, its low toxicity, and high biocompatibility and biodegradability make it an attractive material for biomedical and environmental applications[16].

Due to its band gap energy, ZnO absorbs radiation in the ultraviolet range of the electromagnetic spectrum, making it a suitable material for photocatalytic degradation under UV illumination of water pollutant molecules. In general, the species responsible for the ZnO photocatalytic activity are zinc interstitials, oxygen interstitials, oxygen vacancies, and hydroxyl radicals or radicals from hydrogen peroxide or superoxide produced on the ZnO surface[17].

ZnO can crystallize in three different crystalline structures, such as wurtzite, zinc blende, and rock salt. The hexagonal wurtzite structure is the one thermodynamically stable at room temperature, whereas, zinc blende can generally be obtained by growth on cubic substrates, and the rock salt structure can be obtained only at high pressures[18]. The ZnO wurtzite structure can be described as alternate planes containing tetrahedrally coordinated ions, either Zn^{+2} or O^{-2} ions, leading to the appearance of polar surfaces[19]. The presence of polar surfaces leads to differences in the surface energy and growth rates of different planes during crystallization process, which may benefit the formation of anisotropic morphologies for ZnO, such as nanorods[20,21], nanotubes[22], nanowires[23,24], nanoplates, and nanoflowers[25,26].

The use of ZnO for photocatalytic degradation of tartrazine has been carried out some times in the scientific literature. For instance, Behnajady et al. studied the effects of ZnO load, pH, initial dye concentration, H_2O_2 concentration, light intensity and temperature on tartrazine photocatalytic degradation using commercial ZnO samples[27]. Although the authors did a thorough study regarding the number of variables analyzed, they did not present any information or characterization about the ZnO samples studied in that paper, and how the intrinsic features of the ZnO could influence the photocatalytic process. Vu Anh Tu et al. prepared ZnO nanorods, nanoflowers, and porous nanoparticles and studied the influence of ZnO morphology on photocatalytic degradation of tartrazine[28]. Despite the authors were able to clearly identify the ZnO porous nanoparticles as the best photocatalyst, the photocatalytic experiments were carried out in a single condition, so, not letting to predict if the other morphologies could perform better if some variables like ZnO load or solution initial pH were changed. Türkyılmaz et al. studied the influence of Ni, Mn, Fe, or Ag doping ZnO, and verified that ZnO doped with Ni or Ag presented better photocatalytic tartrazine degradation performance than undoped ZnO[29]. Finally, Modirshahla et al. verified that the tartrazine removal can be improved when the photocatalysis is coupled with an electrocoagulation process[30].

A common feature among all the studies previously mentioned is that all of them were carried out based on the univariate approaches, where each variable is changed at once while the other ones are kept fixed. In opposition to the univariate approach, the multivariate approach has the advantage to study the interaction between factors and the non-linear relations with the responses, performing an amount of experiments smaller than the required by the univariate approach to assess the same information[31].

In this sense, this paper presents a multivariate approach to study the photocatalytic degradation of tartrazine by ZnO nanorods of different aspect ratios. A 2^4 factorial design was carried out having as variables ZnO nanorods aspect ratios, ZnO load, tartrazine solution initial pH, and H_2O_2 volume were studied. From the 16 initial experiments, the variables having meaningful effects on tartrazine removal efficiency and pseudo-1st-order rate constant were identified. Statistical models were obtained allowing to predict the results out of the conditions studied. Comparisons between the results predicted by the models and the results obtained experimentally were carried out by using the response surface methodology.

2. Experimental Procedure:

2.1 Synthesis of ZnO samples with different aspect ratios:

To prepare ZnO_LowAR, in an enclosed bottle were added 35 mL ethanol (200 proof pure ethanol, Koptec), 0.5110 g of zinc acetate dihydrate (ZnAc$_2$.2H$_2$O – Alfa Aesar ACS 98%, 2.33 x 10^{-3} mol), and 1.6200 g of Hexamethylenetetramine (HMTA – Alfa Aesar ACS 99%, 15.5 x 10^{-3} mol), producing a HMTA: Zn^{+2} mole ratio equal to 6.65. The mixture was stirred for 30 minutes at room temperature, then, it was heated at 160 °C for 24 h. After that period, the sample was cooled, centrifuged at 3000 rpm for 5 minutes, and the supernatant was discarded. After the centrifuging procedure, the precipitate was washed with 20 mL ethanol twice and four times with 20 mL H$_2$O, on each washing cycle, the sample was centrifuged, and the supernatant was discarded. The solids were transferred to a petri dish and dried on a hot plate.

To prepare ZnO_HighAR, the procedure was exactly the same, except for the fact that HMTA was completely replaced by 0.4660 g of sodium hydroxide (NaOH - VWR, 11.6 x 10^{-3} mol), producing a NaOH: Zn^{+2} mole ratio equal to 4.98.

2.2 Materials characterization:

For the powder X-ray diffraction (XRD), the samples were pressed onto an aluminum sample holder and the patterns were collected at room temperature in a Shimadzu Lab-X XRD 6000 equipped with CuKα radiation (0.15406 nm), operating at 30 kV and 30 mA, with 2 Θ ranging from 5 to 65˚, with a step size of 0.0200, totaling a time around 2 h of collection per sample. The infrared (IR) spectra were collected in a Thermo Scientific Nicollet 6700 FT-IR spectrometer in the attenuated total reflectance (ATR) mode with the wavenumber between 600 and 4000 cm^{-1} in the solid samples, at room temperature, without additional sample preparation. The UV-vis absorption spectra were collected by dispersing ZnO nanorod powders in methanol by sonication, each spectrum was collected in wavelengths from 190 to 1100 nm, using an Agilent 8453 spectrophotometer. The direct band gap energy was calculated by plotting $(\alpha h\nu)^2$ vs hν (Tauc plot)[32], and extrapolating its linear region to X-axis.

The fluorescence spectra were collected from aqueous dispersions of the powders using a 1 cm path length quartz cuvette. The equipment used was a Hitachi F-4500 Fluorescence Spectrophotometer, using a Xe lamp as excitation source. The excitation wavelength was set to 325 nm, and the emission spectra were scanned from 350 to 600 nm, with a scan speed of 15 nm/min. The emission and excitation slits were set as 5 and 10 nm, respectively. To improve the signal to noise ratio, a Savitzky-Golay smoothing function with 100 points of window and a polynomial of order 5 was applied to each fluorescence spectrum, using the software Origin 2018.

Nitrogen adsorption isotherm for the samples were obtained for a pressure range of $0.01 < P/P_0$ <0.99 at − 196 ℃ with a surface area and porosity analyzer (Tri-Star II 3020, Micromeritics Instrument Corp., Norcross, GA). ZnO nanorod samples were first degassed at 120 ℃ for 3 h

before analysis under 70 mTorr vacuum. The Brunauer–Emmett–Teller (BET) equation was applied to nitrogen adsorption data for P/P_0 between 0.01 and 0.30 to calculate the surface area. Total pore volume was calculated at $P/P_0 = 0.99$. Microporosity of the samples were analyzed with t-plot method.

For scanning electron microscopy (SEM), the ZnO samples were dispersed in methanol, sonicated for 30 min, deposited onto silicon substrates, and the substrate edges were painted with carbon conductive ink to avoid sample charging during imaging. The scanning electron microscope was a Field Emission Gun (FEG) Tescan Mira 3, operating at 10 kV. The particle size distribution was obtained by counting 200 particles manually for each sample with the aid of the software ImageJ[33].

## 2.3 Photocatalytic degradation of tartrazine:

A 25 mg/L aqueous solution of tartrazine was prepared by adding 2.0 mL of a 300 mg/L tartrazine stock solution and 23 mL of deionized water, making up a total of 25 mL of solution. For the experiments using a ZnO load equal to 400 mg/L or 700 mg/L, 10 mg or 17.5 mg of ZnO sample were added, respectively, to the solution. For the experiments at initial pH 7, no pH adjustments were made, whereas for the experiments at initial pH 10, diluted NaOH was added until the initial solution pH equal 10 was reached. Another parameter studied was the volume of H_2O_2, in general, 30 μL H_2O_2 of were added for the experiments requiring H_2O_2.

The solution containing the ZnO powder on the desired load was stirred for 30 minutes in the dark, in order to attain adsorption equilibrium (Figure S1 of Supporting Information). After these 30 minutes, the UV light (UV-Pet Max, emission at 365 nm, and power equal to 120 mW) was turned on with the solution upon stirring, and 2 mL aliquots were collected every 10 minutes for

1 h. The aliquots were centrifuged at 4000 rpm for 20 min. The supernatants were filtered through cotton to determine the tartrazine concentration remaining in solution by tracking the intensity of tartrazine absorption peak at 425 nm using UV-vis spectroscopy.

3. Results

3.1 Microstructural Characterization of ZnO Nanorods:
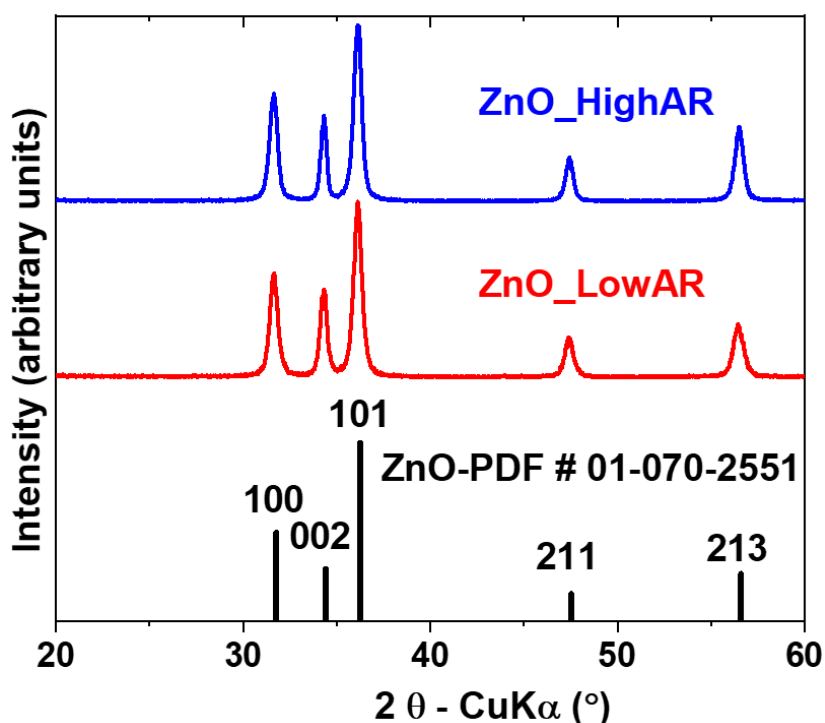
Figure 1. XRD patterns of ZnO reference (bottom), ZnO_LowAR (middle), and ZnO_HighAR (top).

Figure 1 shows the XRD patterns of ZnO_LowAR and ZnO_HighAR, for both samples the hexagonal wurtzite phase of ZnO is observed, agreeing with the PDF card number 01-070-2551. The Scherrer equation[34] by averaging the values calculated for the peaks (100), (002), and (101), revealed crystallite size values equal to 17 and 18 nm, respectively for, ZnO_LowAR and ZnO_HighAR.

The SEM images of ZnO_LowAR and ZnO_HighAR, shown on figure 2 a) and b), respectively, revealed that both samples have a rod-like morphology, however, with visually noticeable different aspect ratios. The particle size distribution histograms of the nanorods show that the ZnO_HighAR has a size range about 5 times higher than the size range of ZnO_LowAR, for the longer dimension (Figure 2 c) and d)). However, the size distribution for the shorter dimension of both samples is very similar, as shown on figure 2 e) and f). For both samples, both the longer and shorter dimension size distributions follow a unimodal gaussian trend, as shown on figure 2 c) to f).
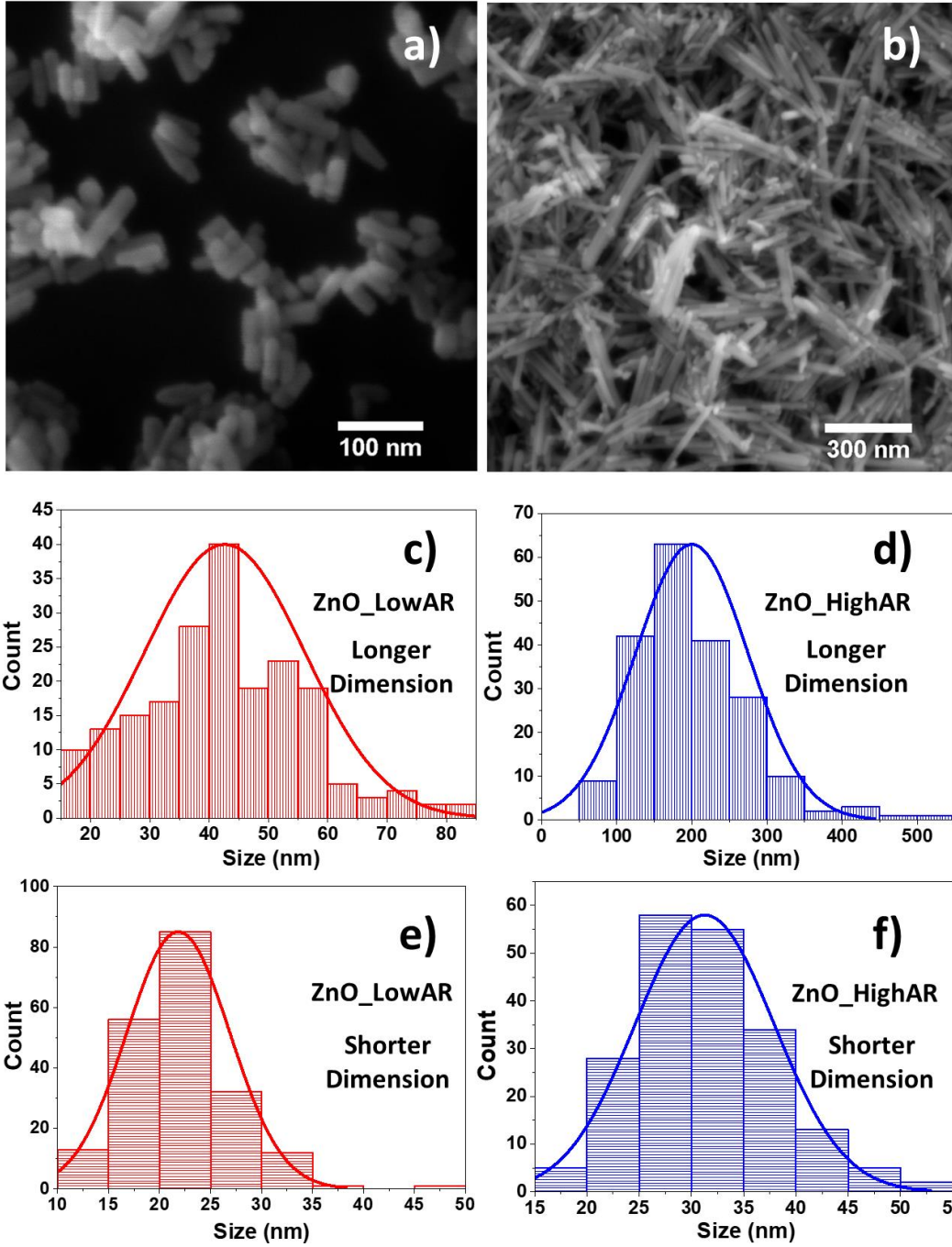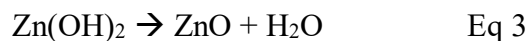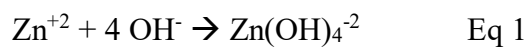
Figure 2. SEM images of a) ZnO_LowAR, b) ZnO_HighAR, Particle size distribution histogram for longer dimension of c) ZnO_LowAR, d) ZnO_HighAR, and Particle size distribution histogram for shorter dimension of e) ZnO_LowAR, f) ZnO_HighAR.

The average size and standard deviation for the longer, shorter dimensions, and the aspect ratio of each one of the ZnO rod samples are shown in Table 1, from these results, one can notice that the ZnO_HighAR has an aspect ratio more than 3 times higher than the aspect ratio of the ZnO_LowAR rod.

Table 1. Average size and standard deviation for longer and shorter dimensions, and aspect ratios for the ZnO_LowAR and ZnO_HighAR

	ZnO_LowAR	ZnO_HighAR
Longer dimension average size (nm)	42 ± 13	200 ± 74
Shorter dimension average size (nm)	21 ± 5	31 ± 6
Aspect ratio	2.0	6.5

The differences in the aspect ratio observed between the two different types of ZnO nanorods can be attributed to the Lewis base, HMTA for ZnO_LowAR and OH^- for ZnO_HighAR, used in the synthetic process of the ZnO nanorods. In general, ZnO solution precipitation can be described by the following sequence of reactions[35,36]:

$$Zn^{+2} + 4\ OH^- \rightarrow Zn(OH)_4^{-2} \qquad \text{Eq 1}$$

$$Zn(OH)_4^{-2} \rightarrow Zn(OH)_2 + 2\ OH^- \qquad \text{Eq 2}$$

$$Zn(OH)_2 \rightarrow ZnO + H_2O \qquad \text{Eq 3}$$

If HMTA is used, the OH- ions are provided by the HMTA decomposition to formaldehyde and ammonia, then, ammonia further hydrolyzes to form NH_4^+ and OH^-. Whereas when NaOH, the OH^- is simply provided by the NaOH dissociation.

When HMTA is used, the OH^- is made available more slowly, it would be a factor limiting the growth of the longer dimension of the nanorods, producing nanorods with lower aspect ratio. Another contributing factor for lower aspect ratio of the nanorods is that ligands like HMTA and NH_3 can coordinate to Zn^{+2} ions, keeping the free Zn^{+2} available in solution in lower concentration to be coordinated to OH^-[37]. Finally, HMTA also has the ability to bind to the nonpolar facets of ZnO nanorods, either by dative covalent bond between its Lewis-basic N donor atom and the Lewis-acidic Zn^{+2} ions or via hydrogen bonding between tertiary ammonium cations and O^{-2} ions. Either interactions mechanism would take to steric hindrance, inhibiting lateral growth, and affecting the growth of the shorter dimension of the nanorods[38].

The N_2 gas adsorption and desorption isotherms for the samples ZnO_LowAR and ZnO_HighAR are shown in Figure 3. Both the isotherms show combined features of type II, III, and IV isotherm according to the IUPAC classification[39]. The shape of the curves suggests none of the materials are highly microporous as there was only small amount of N_2 adsorption at low P/P_0. The absence of proper hysteresis loops between the adsorption and desorption isotherm suggests the materials are not highly mesoporous either[40]. However, the moderate amount of N_2 adsorbed can be attributed to the non-porous surface area and hierarchical porous structure (combination of micro- and mesopores) formed due to aggregation of the nanoparticles[41].
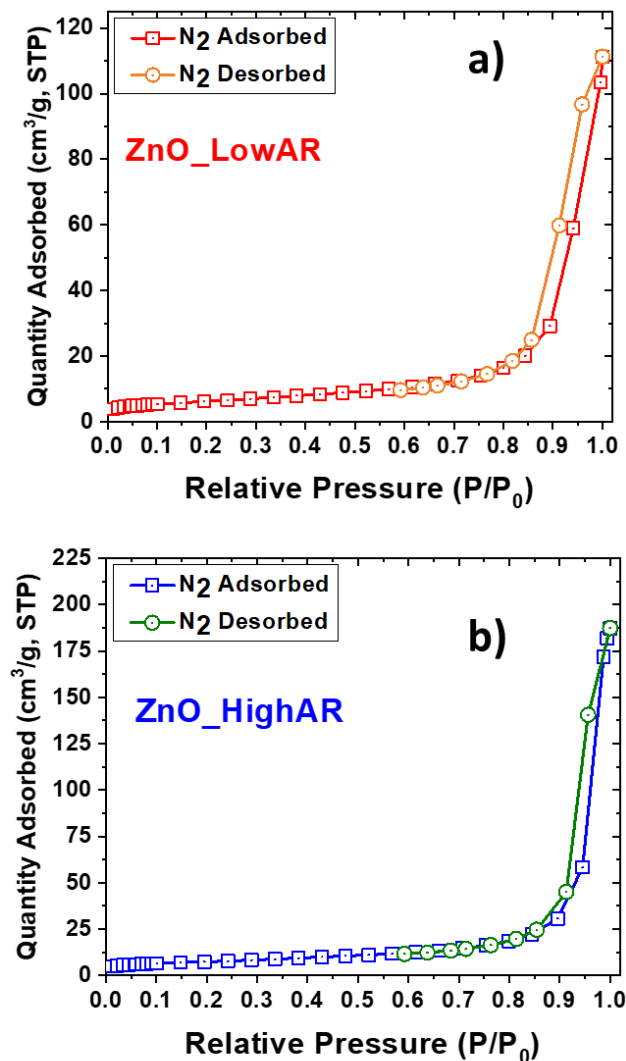
Figure 3. N_2 adsorption isotherm for a) ZnO_LowAR, b) ZnO_HighAR.

The BET surface area plot ($1/[Q(P_0/P - 1)]$ vs P/P_0) for both the samples are shown in Figure S2 of Supporting Information. The plots were linear in that range with correlation coefficient of 0.9999 as per the perquisite of BET surface area calculation. The C (BET constant) value calculated for the ZnO_LowAR and ZnO_HighAR samples were also reasonable, 209.85 and 314.40, respectively. The BET surface area for the samples calculated from the plots were 21.98 and 25.99 m^2/g for ZnO_LowAR and ZnO_HighAR, respectively. These results reveal that the

aspect ratio of the ZnO nanorods does not influence substantially their surface area. It is worth mentioning that the surface areas obtained for both types of nanorods is higher than the ones obtained for other ZnO morphologies. For example, Li *et al.* prepared ZnO rods, disks, screw caps, irregular particles, and rings. The surface area for their samples ranged from 4.5 (for the rods) to 14.11 m²/g (for the irregular particles)[20].

The textural properties, such as BET surface area, single point total pore volume, micropore area, micropore volume, external surface area, and adsorption average pore width are shown in table 2. For all textural properties, the ZnO_HighAR presented higher values. More details about these measurements can be found in Supporting Information section S2 to S4:

Table 2. Textural properties for ZnO_LowAR and ZnO_HighAR samples.

Property	ZnO_LowAR	ZnO_HighAR
BET Surface Area	21.97 m²/g	25.99 m²/g
Single point total pore volume at $P/P_0 = 0.99$	0.16 cm³/g	0.28 cm³/g
Micropore Area (t-Plot)	2.31 m²/g	4.08 m²/g
External Surface Area (t-plot)	19.67 m²/g	21.91 m²/g
Micropore volume (t-plot)	0.0011 cm³/g	0.00194 cm³/g
Adsorption average pore width (4V/A by BET)	29.121 nm	43.28 nm

The UV-vis absorption spectra of ZnO_LowAR and ZnO_HighAR presented an absorption band, respectively, at 367 and 371 nm, as shown in Figure 4 a). The band gap energy for ZnO_LowAR and ZnO_HighAR were 3.19 and 3.22 eV, respectively, as shown in Tauc plot on

Figure 4 b). Although the band gap of bulk ZnO is about 3.37 eV, the lowering of band gap energy in undoped ZnO has been observed in the literature and attributed to factors such as preparatory conditions, presence or absence of oxygen defects, strain, and crystallite size[42,43]. The fluorescence spectra of both ZnO nanorods were very similar with bands around 550 and 560 nm. The presence of two emission bands on that region agrees with the result obtained by van Dijken *et al.*[44]. The first band can be assigned as the transition of a photogenerated electron from a shallow level closer to the conduction band to a deeply trapped hole. Whereas the second band can be assigned as a radiative exciton emission[44].
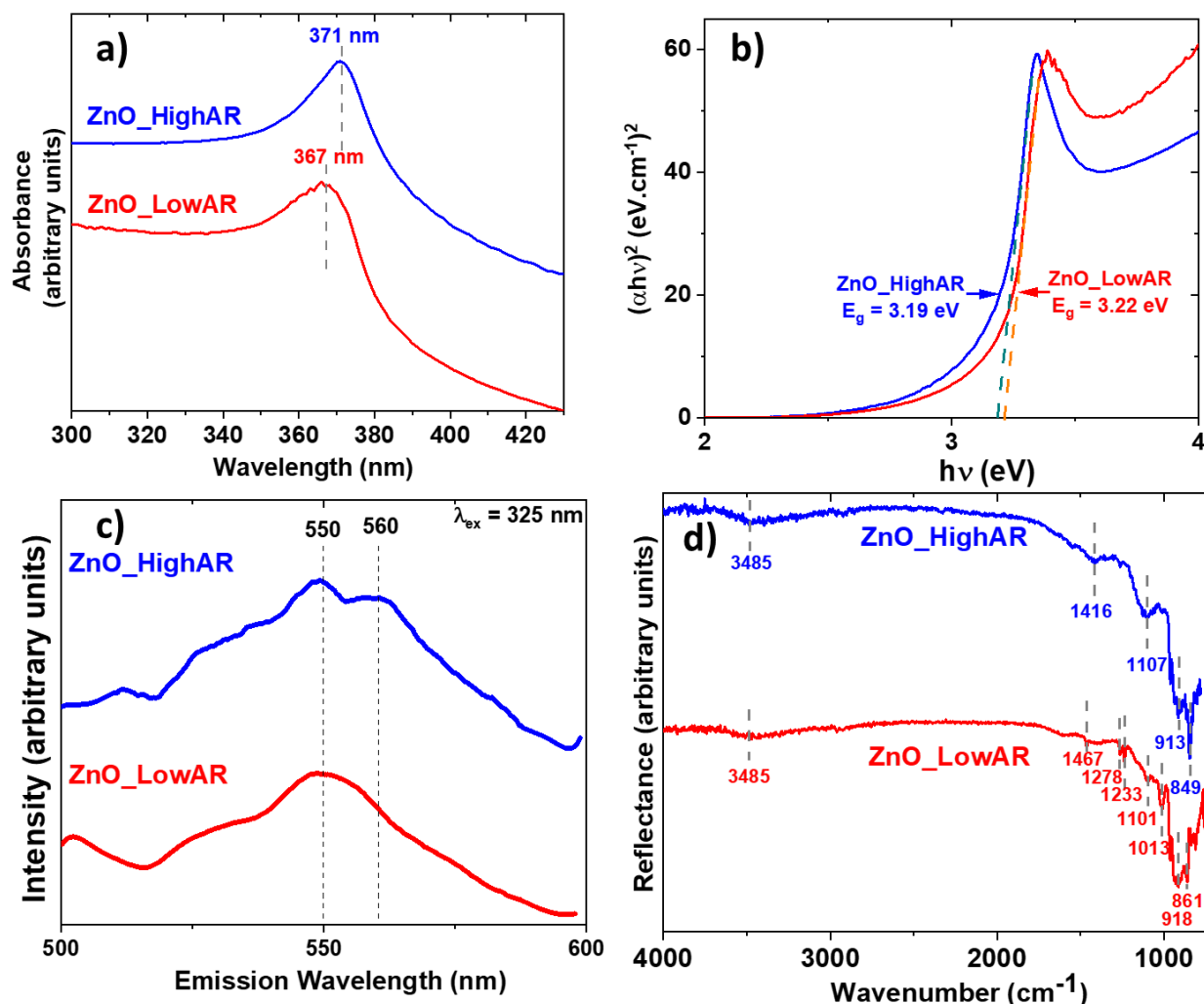
Figure 4. a) UV-vis absorption spectra, b) Tauc plot for band gap estimation, c) fluorescence spectra (excitation wavelength = 325 nm), and d) infrared spectra of ZnO_LowAR and ZnO_HighAR.

The FT-IR-ATR spectra of the ZnO nanorods samples were substantially different, for instance, ZnO_LowAR presented the low intensity peaks located at 1013, 1233, and 1467 cm^{-1}, which can be attributed, respectively, to N-C stretching, CH_2 rocking, and CH_2 scissoring vibrations from HMTA[45]. The other peaks present in the ZnO_LowAR are also present in the ZnO_HighAR, some of them slightly shifted to lower or higher wavenumber. For instance, the peak at 3485 cm^{-1} can be attributed to the H-O stretching vibration probably originated from the ethanol solvent or from

the $Zn(OH)_2$ complexes rendering ZnO (see equation 3)[46]. The peak at 1416 cm^{-1} observed for ZnO_HighAR is related to the symmetric stretching of carboxylate groups from the acetate ion. For the ZnO_LowAR this peak appears alongside the one at 1467 cm^{-1}. The peaks observed at 1107 and 913 cm^{-1} for the ZnO_HighAR are slightly shifted to 1101 and 918 cm^{-1} ZnO_LowAR. These peaks are, respectively, related to stretching of C-OH bonds and twisting of CH_2, which probably originated from fragments of acetate ion or the ethanol solvent[46].

3.2 Factorial Design Variables and Levels:

A 2^4 full factorial design was implemented in order to study the individual and synergistic influence of the ZnO aspect ratio, ZnO load, initial pH of the tartrazine solution, and presence of the H_2O_2 in the tartrazine solution in the removal efficiency and in the pseudo-1st-order rate constant of the photocatalytic degradation of tartrazine by ZnO. The upper level, labelled as 1, and the lower level, labelled as -1, were chosen for each variable are shown in the Table 3:

Table 3. The four variables studied to analyze their impacts in the tartrazine removal efficiency and pseudo-1st-order rate constant in the photocatalytic degradation of tartrazine by ZnO with different aspect ratios.

	Levels	
Variables (Variable Code)	-1	1
ZnO aspect ratio (A)	Low aspect ratio (ZnO_LowAR)	High aspect ratio (ZnO_HighAR)

| ZnO load (B)	400 mg/L	700 mg/L
Initial pH (C)	7	10
H_2O_2 volume (D)	0	30 μL

For the ZnO aspect ratio, the levels were chosen as shown in Table 3 since these were the two types of ZnO nanorods we were interested to study. For the ZnO load, we chose two levels that allowed us to have enough powder from each sample to perform all the 16 required experiments, and also based in other papers from literature that studied the photocatalytic degradation of tartrazine by ZnO[27]. The pH levels were chosen as neutral or mildly alkaline, since it is known that either very acidic pH or very alkaline pH can cause dissolution of ZnO nanomaterials[47], which would completely compromise the heterogeneous feature of the photocatalytic process. The mildly alkaline pH 10 was chosen because it is described in the literature that alkaline pH values can enhance the production of $OH^{\bullet}$ radicals[48], which are able to degrade organic molecules. Finally, the H_2O_2 levels were chosen due to H_2O_2 being an electron acceptor species able to produce $OH^{\bullet}$ radicals[15].

The tartrazine removal efficiency was calculated according to Equation 4:

$$Removal\ Efficiency\ (\%) = \left(1 - \frac{C_t}{C_0}\right) \times 100\% \qquad Eq.\ 4$$

Where the C_0 and C_t are, respectively, the initial tartrazine concentration (mg/L) and the tartrazine concentration (mg/L) remaining in solution in a certain time point.

The combination of the two levels of the four variables produced a total of 16 independent experiments. The experiments produced from each possible combination with the removal efficiency obtained are presented in Figure 5:
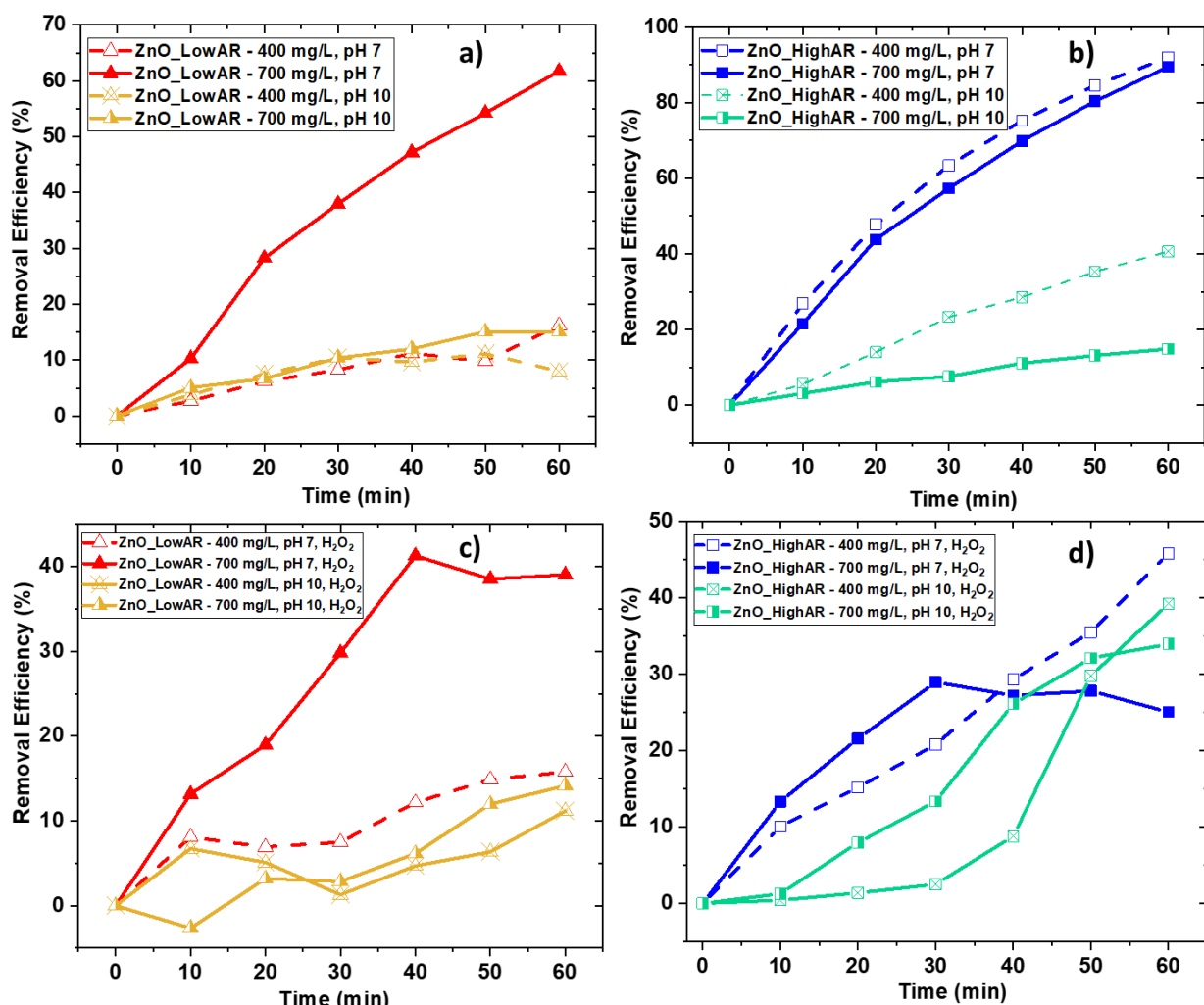
Figure 5. Removal Efficiency versus contact time graphs for a) ZnO_LowAR at varying ZnO load and initial pH, without H_2O_2, b) ZnO_HighAR at varying ZnO load and initial pH, without H_2O_2, c) ZnO_LowAR at varying ZnO load and initial pH, with 30 µL of H_2O_2, d) ZnO_HighAR

The kinetics of photocatalytic degradation of tartrazine by ZnO nanorods were analyzed according to the pseudo-1st-order kinetics model, as described by Equation 5:

$$\ln\left(\frac{c_t}{c_0}\right) = -kt \qquad \text{Eq. 5}$$

Where k is the pseudo-1st-order rate constant (min^{-1}), and t (min) is the time point where the concentration C_t was measured. The pseudo-1st-order rate constant (k) values were calculated from the slop of the linear fit to the experimental data in a graph of ln (C_t/C_0) vs t.

Figure 6 shows the ln (C_t/C_0) vs t plot for all 16 experiments possible from the combination of ZnO aspect ratio, ZnO load, initial pH, and H_2O_2 volume. For all of them, it is possible to verify that all the experiments comply with the pseudo-1st-order kinetics model, as all of them looked like decreasing lines.
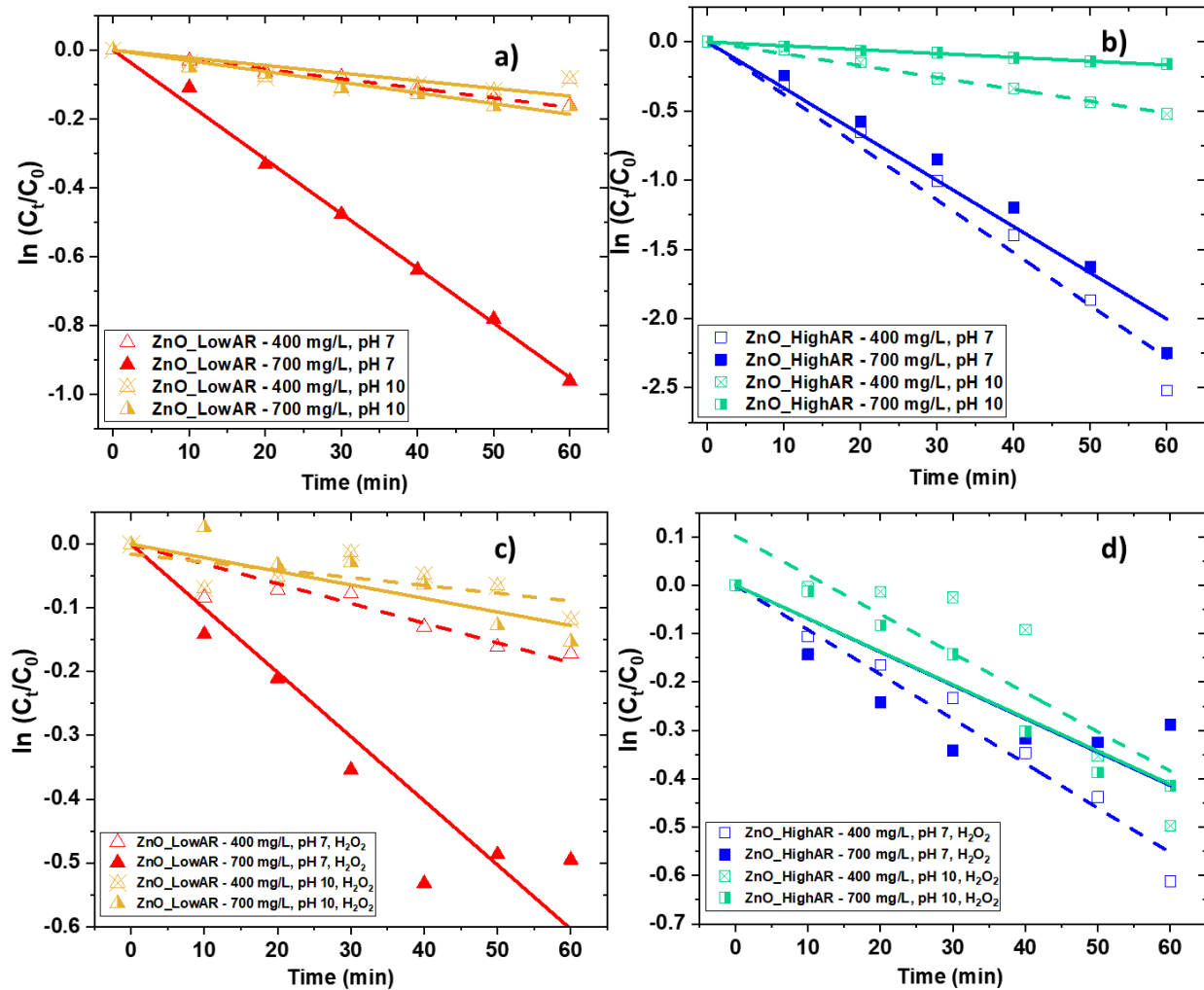
Figure 6. Pseudo-1st-order kinetics graphs for a) ZnO_rods (HMTA) at varying ZnO load and initial pH, without H_2O_2, b) ZnO_fibers (NaOH) at varying ZnO load and initial pH, without H_2O_2,

c) ZnO_rods (HMTA) at varying ZnO load and initial pH, with 30 μL of H_2O_2, d) ZnO_fibers (NaOH) at varying ZnO load and initial pH, with 30 μL of H_2O_2.

The removal efficiency and pseudo-1st-order rate constant values presented, respectively, in Figures 5 and 6, with each variable converted to its coded value is presented in Table 4:

Table 4. Removal Efficiency and pseudo-1st-order rate constant results with the coded variable values for the 16 experiments.

Experiment	A	B	C	D	Removal Efficiency (%)	Rate Constant (min^{-1})
1	-1	-1	-1	-1	17	2.78×10^{-3}
2	1	-1	-1	-1	92	3.81×10^{-2}
3	-1	1	-1	-1	62	1.59×10^{-2}
4	1	1	-1	-1	89	3.34×10^{-2}
5	-1	-1	1	-1	8	2.22×10^{-3}
6	1	-1	1	-1	41	8.58×10^{-3}
7	-1	1	1	-1	15	3.11×10^{-3}
8	1	1	1	-1	15	8.58×10^{-3}
9	-1	-1	-1	1	16	3.11×10^{-3}
10	1	-1	-1	1	46	9.21×10^{-3}
11	-1	1	-1	1	39	3.34×10^{-2}
12	1	1	-1	1	25	6.90×10^{-3}
13	-1	-1	1	1	39	1.23×10^{-3}
14	1	-1	1	1	11	8.10×10^{-3}

15	-1	1	1	1	14	2.13×10^{-3}
16	1	1	1	1	34	6.85×10^{-3}

The highest removal efficiency (92 %) was obtained for Experiment 2, where the ZnO_HighAR with a load of 400 mg/L were used in a solution with an initial pH equal to 7 and without the addition of H_2O_2. In contrast, the lowest removal efficiency (8 %) was obtained for Experiment 5, where the ZnO_LowAR with a load of 400 mg/L were used in a solution with an initial pH equal to 10 and without the addition of H_2O_2. Interestingly, in Experiment 14, where the ZnO_HighAR were used with a load of 400 mg/L at pH 10 with 30 μL of H_2O_2, a comparatively low removal efficiency (11 %) was obtained.

In contrast, the experiments using ZnO_HighAR, in general, presented higher rate constants than the ones using ZnO_LowAR, indicating that photocatalytic degradation of tartrazine happens faster when the ZnO_HighAR are used as photocatalysts. Furthermore, the highest rate constants were obtained at initial pH 7, and in the absence of H_2O_2. As a way to compare the removal efficiency and pseudo-1st-order rate constant of the ZnO nanorods obtained on this paper with a recognized material in the literature, the photocatalytic degradation of tartrazine was carried out using the TiO_2 – P25 as photocatalyst at pH 7, in the absence of H_2O_2, and loads equal to 400 or 700 mg/L. The experiment with load 400 mg/L presented a removal efficiency of 31 % and pseudo-1st-order rate constant of 6.54×10^{-3} min^{-1}. For the same experimental condition (Experiments 1 and 2 on Table 4), the ZnO_HighAR presented better results than TiO_2 – P25 for both response variables. The experiment with load 700 mg/L presented removal efficiency of 58% and pseudo-1st-order rate constant of 1.54×10^{-2} min^{-1}. For the same experimental condition (Experiments 3 and 4 on Table 4), both the ZnO_LowAR and ZnO_HighAR presented better results than TiO_2 –

P25 for both response variables. More details about TiO_2 – P25 results can be seen on Figure S5 in the Supporting Information.

The complexity of the results obtained shows that is misleading to try to understand that the differences in the removal efficiency and pseudo-1st-order rate constant values are based solely on the differences within each variable unconnectedly. Therefore, it is necessary to analyze not only the primary effect of each variable, but also the synergistic effect of combination of the variables based on the concepts of the factorial design of experiments.

As the factorial design contains four variables, it is possible to produce from them four primary effects (A, B, C, and D), six synergistic secondary effects (AB, AC, AD, BC, BD, and CD) from the combination of two variables at time, four tertiary synergistic effects (ABC, ABD, ACD, and BCD) from the combination of three variables at time, and one quaternary synergistic effect (ABCD) from the combination of four variables at time. So, there is a total of 15 effects that can be calculated based on the changing the levels of the variables, and in addition to them there is one effect that is independent on the changing the levels of the variables. In summary, the 2^4 factorial design can be used to produce a mathematical model containing a maximum of 16 parameters, which each one of them is related with the 16 possible effects described[49].

The matrix equations used to calculate the 16 possible effects for removal efficiency and pseudo-1st-order rate constant are presented in the Supporting Information in the section S6 and Equations S1 to S3. The effects obtained by applying Eq S4 and S5 are shown in Table 5:

Table 5. Effect values for Removal Efficiency and rate constant for each variable.

Variable	Effect Values for Removal efficiency (%)	Effect Values for Rate Constant (min^{-1})
Independent	3.5×10^{-1}	1.1×10^{-2}
ZnO aspect ratio (A)	1.8×10^{-1}	7.0×10^{-3}
ZnO load (B)	2.8×10^{-2}	4.6×10^{-3}
Initial pH (C)	-2.6×10^{-1}	-1.3×10^{-2}
H_2O_2 Volume (D)	-1.4×10^{-1}	-5.2×10^{-3}
AB	-9.6×10^{-2}	-6.7×10^{-3}
AC	-1.2×10^{-1}	-1.1×10^{-3}
AD	-1.6×10^{-1}	-9.2×10^{-3}
BC	-8.1×10^{-2}	-4.5×10^{-3}
BD	-2.9×10^{-2}	2.3×10^{-3}
CD	1.9×10^{-1}	4.2×10^{-3}
ABC	1.3×10^{-1}	5.9×10^{-3}
ABD	1.1×10^{-1}	-2.0×10^{-3}
ACD	5.6×10^{-2}	9.1×10^{-3}
BCD	7.1×10^{-2}	-2.6×10^{-3}
ABCD	9.6×10^{-2}	1.7×10^{-3}

To have a better idea of the significance of each effect on the removal efficiency and in the pseudo-1st-order rate constant, their absolute value for each effect was converted to percentage of the summation of the absolute values of all effects, as presented in Figure 7 a) and 7 b), respectively for the effects for removal efficiency and pseudo-1st-order rate constant:
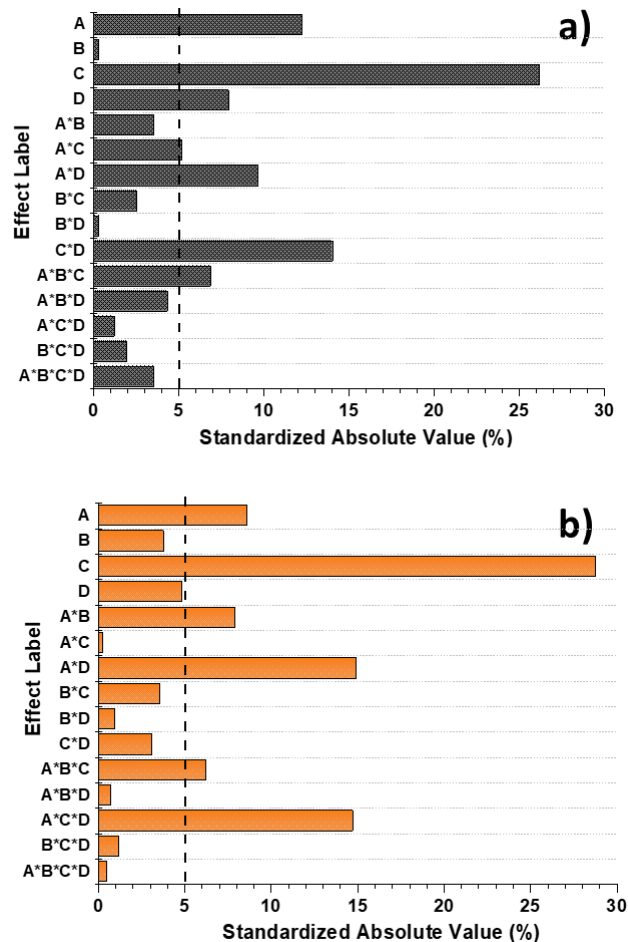
Figure 7. Standardized absolute values for each one of the possible 16 effects for a) removal efficiency, b) pseudo-1st-order rate constant. Effects caption: A = ZnO aspect ratio, B = ZnO load, C = Initial pH, D = H_2O_2 volume.

For the removal efficiency, from Figure 7 a), it is noticed that the initial pH is the variable with highest percent effect (26 %), followed by the ZnO aspect ratio (12 %), and H_2O_2 volume (8 %), whereas, the ZnO load presented a very small effect (0.31 %). The secondary interactions presenting standardized absolute effects higher than 5 % were the combination of ZnO aspect ratio and Initial pH (AC = 5.2 %), the combination of aspect ratio and H_2O_2 Volume (AD = 9.7 %), and the combination of Initial pH and H_2O_2 volume (CD = 14 %). Finally, the tertiary interaction

involving ZnO aspect ratio, ZnO load and Initial pH (ABC) presented a percentage effect around 6.9 %.

For the pseudo-1st-order rate constant, from Figure 7 b), for the primary effects, the trend is the same as presented for the removal efficiency, with the initial pH being the highest one (29 %), followed by the ZnO aspect ratio (8.6 %), and H_2O_2 volume (4.8 %), with the ZnO load being the primary variable having the lowest standardized absolute effect (3.8 %). The secondary interactions presenting standardized absolute effects higher than 5% were the combination of ZnO aspect ratio and load (AB = 7.9 %), and the combination of aspect ratio and H_2O_2 Volume (AD = 15 %). Lastly, the tertiary interactions involving ZnO aspect ratio, ZnO load and Initial pH (ABC = 6.2 %), and ZnO aspect ratio, Initial pH, and H_2O_2 volume (ACD = 15%) were the ones presenting standardized absolute effects higher than 5%.

3.3 Factorial Design Models:

For either response variable (removal efficiency or pseudo-1st-order rate constant), each one of the effects was converted to a coefficient, aiming that after judging the significance of each effect its respective coefficient would be included or not in the equation describing the factorial design mathematical model. The 2^4 factorial design model predicts the obtaining of an equation containing 16 parameters in order to predict the removal efficiency, as described by Eq. 6:

$$Response\ Variable = [\beta_0 + \beta_A X_A + \beta_B X_B + \beta_C X_C + \beta_D X_D + \beta_{AB} X_A X_B + \beta_{AC} X_A X_C +$$
$$\beta_{AD} X_A X_D + \beta_{BC} X_B X_C + \beta_{BD} X_B X_D + \beta_{CD} X_C X_D + \beta_{ABC} X_A X_B X_C + \beta_{ABD} X_A X_B X_D +$$
$$\beta_{BCD} X_B X_C X_D + \beta_{ACD} X_A X_C X_D + \beta_{ABCD} X_A X_B X_C X_D]\ \ \text{Eq. 6}$$

Where the response variable can either be the removal efficiency or the pseudo-1st-order rate constant.

Each one of the β_n coefficients was calculated according to the matrix Eq. 7:

$$\beta_n = \left(\frac{1}{16}\right) [X^t] \times [Y] \text{ Eq 7}$$

Where the $[X^t]$ the transpose of the matrix presented in Eq S1 and $[Y]$ is the matrix represented in Eq. S2 or S3 of Supporting Information.

The coefficients obtained for the effects in the removal efficiency and in the pseudo-1st-order rate constant are shown in Table 6:

Table 6. Removal efficiency model coefficient values obtained from calculation of Eq 7:

Variable	Coefficient for Removal Efficiency Model (%)	Coefficient for pseudo 1st – order Rate Constant Model (min^{-1})
Independent	3.5×10^{-1}	1.1×10^{-2}
ZnO aspect ratio (A)	8.9×10^{-2}	3.5×10^{-3}
ZnO load (B)	1.4×10^{-2}	2.3×10^{-3}
Initial pH (C)	-1.3×10^{-1}	-6.4×10^{-3}
H_2O_2 Volume (D)	-7.2×10^{-2}	-2.6×10^{-3}
AB	-4.8×10^{-2}	-3.3×10^{-3}
AC	-5.8×10^{-2}	-5.6×10^{-4}
AD	-7.9×10^{-2}	-4.6×10^{-3}
BC	-4.1×10^{-2}	-2.2×10^{-3}
BD	-1.4×10^{-2}	1.1×10^{-3}
CD	9.6×10^{-2}	2.1×10^{-3}
ABC	6.7×10^{-2}	3.0×10^{-3}
ABD	5.3×10^{-2}	-1.0×10^{-3}
ACD	2.8×10^{-2}	4.6×10^{-3}
BCD	3.6×10^{-2}	-1.3×10^{-3}

ABCD	4.8×10^{-2}	8.5×10^{-4}

Only the coefficients related to the effects higher than 5 % for either or both of the response variables, as shown in Figure 7, were considered significant. To produce consistent models, the same coefficients will be considered significant for both response variables, in this sense, for both response variables, the models will have the same amount and set of coefficients, allowing a more uniform interpretation of the results. The criteria to consider as significant only the coefficients related to effects higher than 5 % has been successfully adopted in different factorial design papers, where no duplicates were carried out for each experimental condition [50,51].

Four effects were higher than 5% for both response variables: ZnO aspect ratio (A), initial pH (C), the secondary interaction between ZnO aspect ratio and H_2O_2 volume (AD), and the tertiary interaction among ZnO aspect ratio, ZnO load, and initial pH (ABC). Additionally, the H_2O_2 volume (D), and the secondary interactions between ZnO aspect ratio and initial pH (AC), and initial pH and H_2O_2 volume (CD) present effect higher than 5% only for the removal efficiency model. Whereas, for the pseudo-1st-order rate constant the secondary interaction between ZnO aspect ratio and ZnO load, and the tertiary interaction among ZnO aspect ratio, initial pH, and H_2O_2 volume (ACD) also presented effects higher than 5%.

Considering the significant effects for both or either variables, for each response variable, the factorial design model will contain the independent coefficient (β_0) plus the following nine coefficients: β_A, β_C, β_D, β_{AB}, β_{AC}, β_{AD}, β_{CD}, β_{ABC}, and β_{ACD}. So, the model describing the removal efficiency for this 2^4 factorial design is represented by the Eq. 8:

$Removal\ Efficiency(\%) = [0.35 + 0.089X_A - 0.13X_C - 0.072X_D - 0.048X_AX_B -$

$0.058X_AX_C - 0.079X_AX_D + 0.096X_CX_D + 0.067X_AX_BX_C + 0.028X_AX_CX_D] \times (100\%)$

Eq. 8

For the pseudo-1st-order rate constant, the model describing the removal efficiency for this 2^4 factorial design is represented by the Eq. 9:

$k(min^{-1}) = [0.011 + 0.0035X_A - 0.0064X_C - 0.0026X_D - 0.0033X_AX_B - 0.00056X_AX_C -$

$0.0046X_AX_D + 0.0021X_CX_D + 0.0030X_AX_BX_C + 0.0046X_AX_CX_D]$ Eq. 9

3.4 Analysis of Variance (ANOVA) and Model Validation:

By plugging on the Eq. 8 and 9 the coded values (-1 or +1) for each variable for X_A, X_B, X_C, X_D for each experimental condition it was possible to predict removal efficiency and pseudo-1st-order rate constant values based on the obtained model for each response variable and compare them with the values obtained experimentally. The removal efficiency and pseudo-1st-order rate constant values predicted by the model and their respective deviations from the experimental values (present in Table 4) are shown in Table 7:

Table 7. Removal efficiency and pseudo-1st-order rate constant predicted by the model, and their percent errors in comparison to experimental values.

Experiment	X_A	X_B	X_C	X_D	Removal Efficiency Predicted by Model (%)	Percent Error (%)	k Predicted by Model (min^{-1})	Percent Error (%)
1	-1	-1	-1	-1	28	-39.1	3.04 x 10^{-3}	-8.5
2	1	-1	-1	-1	102	-9.5	4.21 x 10^{-2}	-9.4

3	-1	1	-1	-1	51	21.8	1.56×10^{-2}	1.6
4	1	1	-1	-1	79	13.1	2.94×10^{-2}	13.4
5	-1	-1	1	-1	13	-39.8	2.29×10^{-3}	-2.9
6	1	-1	1	-1	26	58.3	8.96×10^{-3}	-4.2
7	-1	1	1	-1	10	57.9	3.05×10^{-3}	2.1
8	1	1	1	-1	30	-49.5	8.20×10^{-3}	4.6
9	-1	-1	-1	1	16	1.9	1.20×10^{-2}	-74.0
10	1	-1	-1	1	47	-1.5	1.44×10^{-2}	-35.8
11	-1	1	-1	1	39	0.8	2.46×10^{-2}	36.0
12	1	1	-1	1	24	5.5	1.75×10^{-3}	293.5
13	-1	-1	1	1	28	37.8	1.30×10^{-3}	-5.3
14	1	-1	1	1	21	-46.3	7.86×10^{-3}	3.1
15	-1	1	1	1	25	-42.8	2.06×10^{-3}	3.5
16	1	1	1	1	24	39.9	7.10×10^{-3}	-3.5

For the removal efficiency, in general, the lowest percent errors were obtained for the experiments at initial pH 7 and 30 µL of H_2O_2 (experiments 9 to 12), whereas the highest percent errors were obtained for the experiments at initial pH 10, either with 0 µL of H_2O_2 (experiments 5 to 8) or with 30 µL of H_2O_2 (experiments 13 to 16). For the pseudo-1st-order rate constant, most experiments presented percent errors lower than 15%, except for the experiments where the initial pH was 7 and with 30 µL of H_2O_2 (experiments 9 to 12). These results indicate that for both response variables, in general, there is a lower agreement with the experimental data when H_2O_2 is present in the experiment. Also, it is important to be attentive to the result predicted by the model for the removal efficiency in the Experiment 2, which was slightly higher than 100%. As the models obtained by factorial design are build up based on purely statistical concepts without

inserting any boundary condition to fit the chemistry context, readers should interpret that result as being as close as possible to 100%, since it is known that removal efficiencies higher than 100% are not chemically allowed. It is worth mentioning that small discrepancies like this do not invalidate the conclusions drawn from the models obtained.

To determine the suitability of the models, three parameters called sum of squares (SS) were calculated, they are: the sum of square (SS) for the mean, for the regression, and for the residuals were defined according to Eq. 10 to Eq. 12:

$$SS_{mean} = \sum \left(Response_{Exp} - Mean\ Response_{Exp} \right)^2 \qquad \text{Eq. 10}$$

$$SS_{regression} = \sum \left(Response_{Predicted} - Mean\ Response_{Exp} \right)^2 \qquad \text{Eq. 11}$$

$$SS_{residual} = \sum \left(Response_{Exp} - Response_{Predicted} \right)^2 \qquad \text{Eq. 12}$$

On equation Eq. 10 to Eq. 12 the terms $Response_{exp}$ and $Response_{predicted}$ represent, respectively, the removal efficiency or pseudo-1st-order rate constant obtained experimentally and their values predicted by the models described by Eq 8 or Eq 9.

Each sum of square has a certain number of degrees of freedom associated to them, for $SS_{residual}$ the number of degrees of freedom is equal the difference of the number of independent experiments (16) and the number of parameters contained in the equation describing the model (10), so $SS_{residual}$ has 10 degrees of freedom. For the $SS_{regression}$ the number of degrees of freedom is equal to the number of parameters (10) minus 1, so the $SS_{regression}$ has 9 degrees of freedom. Finally, the number of degrees of freedom of SS_{mean} is equal to the number of degrees of freedom for $SS_{residual}$ and $SS_{regression}$, so 15 degrees of freedom. The square mean (SM) for regression, residual, and mean was calculated by dividing each sum of square by its respective number of degrees of freedom.

The SS results obtained are summarized in the Analysis of variance (ANOVA) table, shown in the Tables 8 and 9, respectively for the removal efficiency and pseudo-1st-order rate constant:

**Table 8.** ANOVA table for the model obtained for removal efficiency

ANOVA Table			
Source of variation	Sum of Square	Degrees of Freedom	Square Mean
Mean	10414.44	15	694.30
Regression	9025.04	9	1002.78
Residual	1356.08	6	226.01
R^2 ($SS_{regression}/SS_{mean}$)	0.87		
$SM_{regression}/SM_{residual}$	4.44		
F-test for 9/6 degrees of freedom with 95%	4.10		

Table 9. ANOVA table for the model obtained for pseudo-1st-order rate constant

ANOVA Table			
Source of variation	Sum of Square	Degrees of Freedom	Square Mean
Mean	2.26×10^{-3}	15	1.50×10^{-4}
Regression	2.02×10^{-3}	9	2.24×10^{-4}
Residual	2.41×10^{-4}	6	4.02×10^{-5}
R^2 ($SS_{regression}/SS_{mean}$)	0.89		
$SM_{regression}/SM_{residual}$	5.58		
F-test for 9/6 degrees of freedom with 95%	4.10		

To test the quality of the model proposed, two parameters were used, the first one is the R^2, which is the ratio between $SS_{regression}$ and SS_{mean}. R^2 values equal to 0.87 and 0.89 were obtained for the removal efficiency and rate constant models, respectively, revealing that 87% and 89% of the variation obtained can be suitably explained by each model. The second parameter is obtained by calculating the ratio between $SM_{regression}$ and $SM_{residual}$ and comparing this value with the F-test value with 9 degrees of freedom for the numerator and 6 degrees of freedom for the denominator and 95% of confidence. As the ratios $SM_{regression}/SM_{residual}$ for both models are higher than $F_{9,6}$ (4.10), we can consider that the model is properly adjusted to the data.

To generalize the model, response surface graphs were plotted for each one of the aspect ratios studied for the ZnO nanorods (variable ZnO aspect ratio (A) = -1 (for ZnO_lowAR) and 1 (for ZnO_HighAR), by fixing the ZnO load equal to 400 mg/L (B = -1), and varying the initial pH between 7 and 10 (coded values -1 and 1, respectively), and H_2O_2 volume between 0 and 30 µL (coded values -1 and 1, respectively). The response surface graphs for ZnO_lowAR and 1 for ZnO_highAR are shown, respectively, at Figure 8 a) and 8 b), for removal efficiency and 8 c) and 8 d) for pseudo-1st-order rate constant.
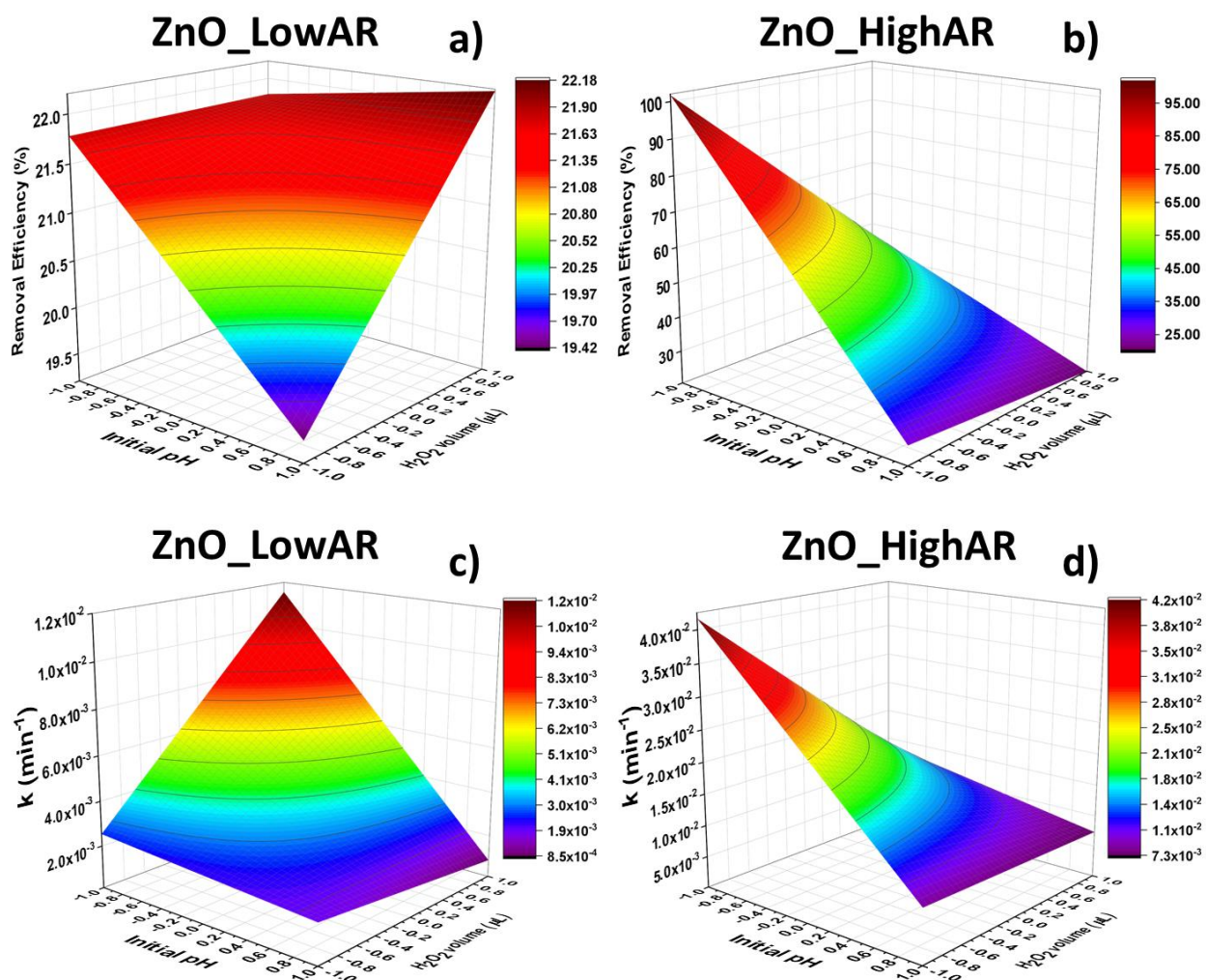
Figure 8. Response Surface graphs a) Removal Efficiency for ZnO_LowAR, b) Removal Efficiency ZnO_HighAR, c) pseudo-1st-order rate constant for ZnO_LowAR, d) pseudo-1st-order rate constant for ZnO_HighAR.

Regarding removal efficiency, the ZnO_LowAR and ZnO_HighAR follow different trends. For instance, under the conditions studied by the response surface, the highest removal for ZnO_LowAR is lower than 25%, whereas for ZnO_HighAR it is very close to 100%. For the ZnO_LowAR, the highest removal can be attained either at pH as close to 7 and 0 μL of H_2O_2

(coded values equal -1 for initial pH and H_2O_2 volume), or when the pH is as close as to 10 and H_2O_2 volume as close as 30 μL (coded values 1 for initial pH and H_2O_2 volume), or yet when the initial pH is as close as to 7 and H_2O_2 volume as close as 30 μL (coded value -1 for initial pH and 1 for H_2O_2 volume). Conversely, for the ZnO_HighAR the highest removal efficiency can be attained only when the initial pH is as close as to 7 and 0 μL of H_2O_2 (coded values equal -1 for initial pH and H_2O_2 volume).

Regarding the pseudo-1st-order rate constant, again the ZnO_HighAR presented higher values than ZnO_LowAR under the conditions studied by the response surface graph. For instance, the maximum pseudo-1st-order rate constant for ZnO_HighAR is around 4.0×10^{-2} min^{-1}, against 1.2×10^{-3} min^{-1} for ZnO_LowAR. For ZnO_HighAR the conditions to maximize the rate constant were the same ones to maximize the removal efficiency, initial pH is as close as to 7 and 0 μL of H_2O_2 (coded values equal -1 for initial pH and H_2O_2 volume). Whereas for ZnO_LowAR, the pseudo-1st-order rate constant could be maximized only when the initial pH is as close as to 7 and H_2O_2 volume as close as 30 μL (coded value -1 for initial pH and 1 for H_2O_2 volume).

To validate the trends described by the response surface graphs and the equation describing the model (Eq. 8 and 9), four previously untested conditions were chosen to compare the results predicted by the Eq. 8 and 9 and surface response graphs shown in Figure 9. In the first condition, the ZnO_LowAR ($X_A = -1$) was used, with a load equal to 400 mg/L ($X_B = -1$), initial pH equal 7 ($X_C = -1$), and H_2O_2 volume equal to 15 μL ($X_D = 0$). In the second condition, the ZnO_HighAR ($X_A = 1$) was used, with a load equal to 400 mg/L ($X_B = -1$), initial pH equal 7 ($X_C = -1$), and H_2O_2 volume equal to 15 μL ($X_D = 0$). In the third and fourth conditions, ZnO_LowAR and ZnO_HighAR were, respectively, used, whereas the load was equal to 400 mg/L ($X_B = -1$), initial

pH (8.5, $X_C = 0$), and H_2O_2 volume (30 μL, $X_D = 1$) were chosen. The results obtained are summarized in tables 10 and 11:

Table 10. Experimental removal efficiency, removal efficiency predicted by the model and percent error for four conditions previously untested.

Experiment	X_A	X_B	X_C	X_D	Exp. Removal Efficiency (%)	Removal Efficiency Predicted by Model (%)	% Error
17	-1	-1	-1	0	20	22	-8.3
18	1	-1	-1	0	37	74	-50.1
19	-1	-1	0	1	17	22	-22.7
20	1	-1	0	1	38	34	13.1

Table 11. Experimental pseudo-1st-order rate constant, experimental pseudo-1st-order rate constant predicted by the model and percent error for four conditions previously untested.

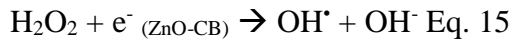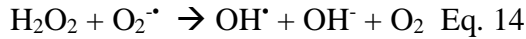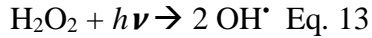| Experiment	X_A	X_B	X_C	X_D	Exp. k (min^{-1})	k Predicted by Model (min^{-1})	% Error
17	-1	-1	-1	0	3.80×10^{-3}	7.49×10^{-3}	-49.3
18	1	-1	-1	0	8.14×10^{-3}	2.82×10^{-2}	-71.1
19	-1	-1	0	1	3.29×10^{-3}	6.62×10^{-3}	-50.3
20	1	-1	0	1	1.01×10^{-2}	1.11×10^{-2}	-9.1

For the ZnO_LowAR, the best agreement between the model and experimental data was obtained when the initial pH was 7 and H_2O_2 volume equal to 15 μL (experiment 17), for removal efficiency the model predicted only 2% more than the experiment result (% error only -8.3%),

whereas for the pseudo-1st-order rate constant, the model predicted approximately the double of the experimentally obtained result, it can infer that the model provided a reasonable estimate on this case, since the result is within the same order of magnitude of the experimental result. About the ZnO_HighAR, the best agreement between the model and experimental data was obtained when the initial pH was 8.5 and H$_2$O$_2$ volume equal to 30 µL (experiment 20), for the removal efficiency the model underestimated the experimental value for only 4% (% error only 13.1%), whereas the pseudo-1st-order rate constant was overestimated for less than 10%.
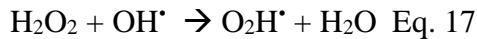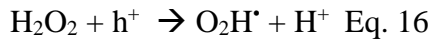
4. Discussions:

The ZnO nanorod aspect ratio is an important variable, since due to the anisotropic nature of the nanorods, facets from different polarities can be exposed on the nanorods surfaces. If polar facets like {0001} are exposed in the surface of the nanorod, it will lead to an improvement in the photocatalytic activity, in comparison to semipolar facets like {10$\bar{1}$1} or nonpolar facets like {10$\bar{1}$0}[52]. Huang *et al.* prepared ZnO nanorods similar to the ZnO_LowAR, also using HMTA to control the morphology, and they concluded that the dominant facet in the rod sides surface was the nonpolar {10$\bar{1}$0}[52]. In contrast, Li *et al.* prepared ZnO nanorods with aspect ratio 8.6, starting from zinc acetate and NaOH, like the ZnO_HighAR prepared in the present paper, and observed the predominance of the polar facets {0001} in the rod sides surface[53]. The possible predominance of polar facets {0001} in the ZnO_HighAR, in comparison to the possible predominance of nonpolar facets {10$\bar{1}$0} in the ZnO_LowAR could help to explain the higher removal efficiency and pseudo-1st-order rate constant for ZnO_HighAR, since there is not a large difference in the surface area of both samples.

The interaction between ZnO aspect ratio and H_2O_2 volume is an important secondary interaction to the model, since it revealed that when H_2O_2 is absent, in general, the ZnO_HighAR presented higher removal efficiency and pseudo-1st-order rate constant than the respective experiments using ZnO_LowAR. Then, when 30 μL H_2O_2 is used there is a balance between the two types of nanorods regarding which one presents higher removal efficiency and pseudo-1st-order rate constant. The meaningfulness of H_2O_2 volume as primary interaction, and as secondary interaction either with ZnO aspect ratio or initial pH, and as tertiary interaction with ZnO aspect ratio and initial pH is based on the fact that H_2O_2 has the capability to produce OH˙radicals, which have the ability to degrade the organic molecule, by different means. The first one is through direct photolysis of H_2O_2 by UV radiation, as shown in equation 13, the second one is by reacting with $O_2^{-˙}$ radicals, as shown by equation 14, and the third one is serving as electron acceptor by taking the electrons present in the ZnO conduction band, as shown in equation 15[17]:

$$H_2O_2 + h\nu \rightarrow 2\ OH˙ \quad \text{Eq. 13}$$

$$H_2O_2 + O_2^{-˙} \rightarrow OH˙ + OH^- + O_2 \quad \text{Eq. 14}$$

$$H_2O_2 + e^-_{(ZnO\text{-}CB)} \rightarrow OH˙ + OH^- \quad \text{Eq. 15}$$

However, depending on how much H_2O_2 is used, it can act also as a scavenger for holes or OH˙ radicals, as shown in equations 16 and 17, respectively. The free radicals also can react producing neutral species, as shown in equation 18, which do not have ability to degrade the organic molecules[17]:

$$H_2O_2 + h^+ \rightarrow O_2H˙ + H^+ \quad \text{Eq. 16}$$

$$H_2O_2 + OH˙ \rightarrow O_2H˙ + H_2O \quad \text{Eq. 17}$$

$$O_2H˙ + OH˙ \rightarrow O_2 + H_2O \quad \text{Eq. 18}$$

In this sense, it can have either no improvement or even a detrimental result in the organic molecule photocatalytic degradation[15]. This was probably the reason why increasing the H_2O_2 volume from 0 to 30 μL led to a negative effect both for the removal efficiency and for the pseudo-1st-order rate constant, as observed in the Table 5.

Particular attention should be paid to the initial pH, as it was the variable with highest standardized absolute effect value according to Figure 7. Also, according to Table 5, the initial pH presented negative effect values, both for the removal efficiency and the pseudo-1st-order rate constant, which means that increasing the pH from 7 to 10, led to a decrease for both response variables. Tartrazine molecule has three types of acidic H^+ ions, the $-SO_3^-$, the $-COO^-$, and the OH^-, the pKa of each group is, respectively, around 2.0, 5.0, and 9.5[54,55]. So, at pH 7, the tartrazine molecule can be considered a monoprotic acid, with overall charge -3, as we abbreviate as $HTart^{-3}$. Then, at pH 10, there is an equilibrium between the protonated ($HTart^{-3}$) and the deprotonated ($Tart^{-4}$) forms. Recently, Rashidi et al. determined that at pH 10, the tartrazine contains about 40 % of the $Tart^{-4}$ at pH 10[55]. The $Tart^{-4}$ has a resonance structure, as shown in Figure 9, which confers to it a higher stability than $HTart^{-3}$, and then, less susceptible to be degraded by photocatalytic means[55]. In summary, although mildly alkaline pH was expected to produce more $OH^\bullet$ radicals[48], it also led the tartrazine molecule to a more stable form, which in turn made it more difficult to be degraded.
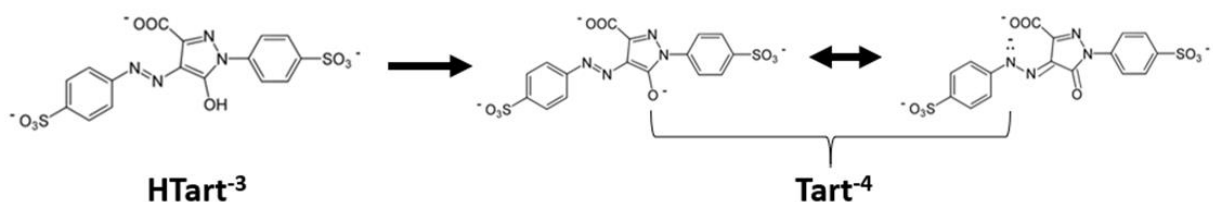
Figure 9. Tartrazine deprotonation scheme at pH around 9.5 and the resonance structures of the fully deprotonated form of tartrazine ($Tart^{-4}$).

5. Conclusions:

The statistical models derived from the 2^4 factorial design revealed that both the removal efficiency and pseudo-1st-order rate constant are independent of the ZnO load, in the conditions studied. However, they are dependent on the ZnO aspect ratio, initial pH of the tartrazine solution, and volume of H_2O_2. The best removal efficiency and pseudo-1st-order rate constant were obtained when the ZnO_HighAR is used at pH close to 7 and in the absence of H_2O_2. The possible reasons for this condition to present the highest performance are the predominance of polar facets {0001} in the ZnO_HighAR, the H_2O_2 acting either as a hole or OH$^{\bullet}$ radical scavenger, and predominance of the protonated form of tartrazine, which is more susceptible to degradation, at pH 7.

Supporting Information:

Supporting Information file is provided free of charge containing adsorption equilibrium graph, detailed textural characterization of ZnO nanorods samples, photocatalysis experiments with TiO_2-P25, factorial design effects calculation.

Corresponding Author:

Alexandre H. Pinto - Department of Chemistry & Biochemistry, Manhattan College, 4513 Manhattan College Parkway, Riverdale, NY 10471, USA – alex.pinto@manhattan.edu.

Author Contributions

The manuscript was written through contributions of all authors. All authors have given approval to the final version of the manuscript.

Notes

References:

(1)   Mekonnen, M. M.; Hoekstra, A. Y. Four Billion People Facing Severe Water Scarcity. *Sci. Adv.* **2016**, *2* (2), 1–7. https://doi.org/10.1126/sciadv.1500323.

(2)   Chen, B.; Han, M. Y.; Peng, K.; Zhou, S. L.; Shao, L.; Wu, X. F.; Wei, W. D.; Liu, S. Y.; Li, Z.; Li, J. S.; et al. Global Land-Water Nexus: Agricultural Land and Freshwater Use Embodied in Worldwide Supply Chains. *Sci. Total Environ.* **2018**, *613–614*, 931–943. https://doi.org/10.1016/j.scitotenv.2017.09.138.

(3)   Duan, K.; Caldwell, P. V.; Sun, G.; McNulty, S. G.; Zhang, Y.; Shuster, E.; Liu, B.; Bolstad, P. V. Understanding the Role of Regional Water Connectivity in Mitigating Climate Change Impacts on Surface Water Supply Stress in the United States. *J. Hydrol.* **2019**, *570* (January), 80–95. https://doi.org/10.1016/j.jhydrol.2019.01.011.

(4)   Schwarzenbach, R. P.; Egli, T.; Hofstetter, T. B.; von Gunten, U.; Wehrli, B. Global Water Pollution and Human Health. *Annu. Rev. Environ. Resour.* **2010**, *35* (1), 109–136. https://doi.org/10.1146/annurev-environ-100809-125342.

(5)   Forgacs, E.; Cserháti, T.; Oros, G. Removal of Synthetic Dyes from Wastewaters: A Review. *Environ. Int.* **2004**, *30* (7), 953–971. https://doi.org/10.1016/j.envint.2004.02.001.

(6)   Bafana, A.; Devi, S. S.; Chakrabarti, T. Azo Dyes: Past, Present and the Future. *Environ. Rev.* **2011**, *19* (NA), 350–371. https://doi.org/10.1139/a11-018.

(7)   Xu, H.; Yang, X.; Li, G.; Zhao, C.; Liao, X. Green Synthesis of Fluorescent Carbon Dots for Selective Detection of Tartrazine in Food Samples. *J. Agric. Food Chem.* **2015**, *63* (30), 6707–6714. https://doi.org/10.1021/acs.jafc.5b02319.

(8)   Dotto, G. L.; Vieira, M. L. G.; Pinto, L. A. A. Kinetics and Mechanism of Tartrazine Adsorption onto Chitin and Chitosan. *Ind. Eng. Chem. Res.* **2012**, *51* (19), 6862–6868. https://doi.org/10.1021/ie2030757.

(9)   Shan, G.; Yan, S.; Tyagi, R. D.; Surampalli, R. Y.; Zhang, T. C. Applications of Nanomaterials in Environmental Science and Engineering: Review. *Pract. Period. Hazardous, Toxic, Radioact. Waste Manag.* **2009**, *13* (2), 110–119. https://doi.org/10.1061/(ASCE)1090-025X(2009)13:2(110).

(10)   Liu, B.; Zhao, X.; Terashima, C.; Fujishima, A.; Nakata, K. Thermodynamic and Kinetic Analysis of Heterogeneous Photocatalysis for Semiconductor Systems. *Phys. Chem. Chem. Phys.* **2014**, *16* (19), 8751–8760. https://doi.org/10.1039/c3cp55317e.

(11)   Ohtani, B. Revisiting the Fundamental Physical Chemistry in Heterogeneous Photocatalysis: Its Thermodynamics and Kinetics. *Phys. Chem. Chem. Phys.* **2014**, *16* (5), 1788–1797. https://doi.org/10.1039/c3cp53653j.

(12)   Shakir, M.; Faraz, M.; Sherwani, M. A.; Al-Resayes, S. I. Photocatalytic Degradation of the Paracetamol Drug Using Lanthanum Doped ZnO Nanoparticles and Their In-Vitro Cytotoxicity Assay. *J. Lumin.* **2016**, *176*, 159–167.

https://doi.org/10.1016/j.jlumin.2016.03.027.

(13)   Elmolla, E. S.; Chaudhuri, M. Degradation of Amoxicillin, Ampicillin and Cloxacillin Antibiotics in Aqueous Solution by the UV/ZnO Photocatalytic Process. *J. Hazard. Mater.* **2010**, *173* (1–3), 445–449. https://doi.org/10.1016/j.jhazmat.2009.08.104.

(14)   Chakrabarti, S.; Dutta, B. K. Photocatalytic Degradation of Model Textile Dyes in Wastewater Using ZnO as Semiconductor Catalyst. *J. Hazard. Mater.* **2004**, *112* (3), 269–278. https://doi.org/10.1016/j.jhazmat.2004.05.013.

(15)   Navarro, S.; Fenoll, J.; Vela, N.; Ruiz, E.; Navarro, G. Photocatalytic Degradation of Eight Pesticides in Leaching Water by Use of ZnO under Natural Sunlight. *J. Hazard. Mater.* **2009**, *172* (2–3), 1303–1310. https://doi.org/10.1016/j.jhazmat.2009.07.137.

(16)   Kolodziejczak-Radzimska, A.; Jesionowski, T. Zinc Oxide-from Synthesis to Application: A Review. *Materials (Basel).* **2014**, *7* (4), 2833–2881. https://doi.org/10.3390/ma7042833.

(17)   Kumar, S. G.; Rao, K. S. R. K. Zinc Oxide Based Photocatalysis: Tailoring Surface-Bulk Structure and Related Interfacial Charge Carrier Dynamics for Better Environmental Applications. *RSC Adv.* **2015**, *5* (5), 3306–3351. https://doi.org/10.1039/C4RA13299H.

(18)   Özgür, Ü.; Alivov, Y. I.; Liu, C.; Teke, A.; Reshchikov, M. A.; Doğan, S.; Avrutin, V.; Cho, S. J.; Morkọ, H. A Comprehensive Review of ZnO Materials and Devices. *J. Appl. Phys.* **2005**, *98* (4), 1–103. https://doi.org/10.1063/1.1992666.

(19)   Wang, Z. L. Zinc Oxide Nanostructures: Growth, Properties and Applications. *J. Phys. Condens. Matter* **2004**, *16*, R829–R858. https://doi.org/10.1088/0953-8984/16/25/R01.

(20)   Li, G. R.; Hu, T.; Pan, G. L.; Yan, T. Y.; Gao, X. P.; Zhu, H. Y. Morphology-Function

Relationship of ZnO: Polar Planes, Oxygen Vacancies, and Activity. *J. Phys. Chem. C* **2008**, *112* (31), 11859–11864. https://doi.org/10.1021/jp8038626.

(21)   Jeong, H. W.; Choi, S. Y.; Hong, S. H.; Lim, S. K.; Han, D. S.; Abdel-Wahab, A.; Park, H. Shape-Dependent Charge Transfers in Crystalline ZnO Photocatalysts: Rods versus Plates. *J. Phys. Chem. C* **2014**, *118* (37), 21331–21338. https://doi.org/10.1021/jp506032f.

(22)   Chu, D.; Masuda, Y.; Ohji, T.; Kato, K. Formation and Photocatalytic Application of ZnO Nanotubes Using Aqueous Solution. *Langmuir* **2010**, *26* (4), 2811–2815. https://doi.org/10.1021/la902866a.

(23)   Yuhas, B. D.; Zitoun, D. O.; Pauzauskie, P. J.; He, R.; Yang, P. Transition-Metal Doped Zinc Oxide Nanowires. *Angew. Chemie - Int. Ed.* **2006**, *45* (3), 420–423. https://doi.org/10.1002/anie.200503172.

(24)   Šutka, A.; Käämbre, T.; Pärna, R.; Juhnevica, I.; Maiorov, M.; Joost, U.; Kisand, V. Co Doped ZnO Nanowires as Visible Light Photocatalysts. *Solid State Sci.* **2016**, *56*, 54–62. https://doi.org/10.1016/j.solidstatesciences.2016.04.008.

(25)   Desai, M. A.; Sartale, S. D. Facile Soft Solution Route to Engineer Hierarchical Morphologies of ZnO Nanostructures. *Cryst. Growth Des.* **2015**, *15* (10), 4813–4820. https://doi.org/10.1021/acs.cgd.5b00561.

(26)   Zhang, H.; Yang, D.; Ji, Y. J.; Ma, X. Y.; Xu, J.; Que, D. L. Low Temperature Synthesis of Flowerlike ZnO Nanostructures by Cetyltrimethylammonium Bromide-Assisted Hydrothermal Process. *J. Phys. Chem. B* **2004**, *108* (13), 3955–3958. https://doi.org/10.1021/jp036826f.

(27) Behnajady, M. A.; Modirshahla, N.; Hamzavi, R. Kinetic Study on Photocatalytic Degradation of C.I. Acid Yellow 23 by ZnO Photocatalyst. *J. Hazard. Mater.* **2006**, *133* (1–3), 226–232. https://doi.org/10.1016/j.jhazmat.2005.10.022.

(28) Tu, V. A.; Tuan, V. A. A Facile and Fast Solution Chemistry Synthesis of Porous ZnO Nanoparticles for High Efficiency Photodegradation of Tartrazine. **2018**, *56* (3), 214–219. https://doi.org/10.1002/vjch.201800016.

(29) Türkyılmaz, Ş. Ş.; Güy, N.; Özacar, M. Photocatalytic Efficiencies of Ni, Mn, Fe and Ag Doped ZnO Nanostructures Synthesized by Hydrothermal Method: The Synergistic/Antagonistic Effect between ZnO and Metals. *J. Photochem. Photobiol. A Chem.* **2017**, *341*, 39–50. https://doi.org/10.1016/j.jphotochem.2017.03.027.

(30) Modirshahla, N.; Abdoli, M.; Behnajady, M. A.; Vahid, B. Decolourization of Tartrazine from Aqueous Solutions by Coupling Electrocoagulation with ZnO Photocatalyst. *Environ. Prot. Eng.* **2013**, *39* (1), 59–73. https://doi.org/10.5277/EPE130105.

(31) Vera Candioti, L.; De Zan, M. M.; Cámara, M. S.; Goicoechea, H. C. Experimental Design and Multiple Response Optimization. Using the Desirability Function in Analytical Methods Development. *Talanta* **2014**, *124*, 123–138. https://doi.org/10.1016/j.talanta.2014.01.034.

(32) Della Gaspera, E.; Chesman, A. S. R.; Van Embden, J.; Jasieniak, J. J. Non-Injection Synthesis of Doped Zinc Oxide Plasmonic Nanocrystals. *ACS Nano* **2014**, *8* (9), 9154–9163. https://doi.org/10.1021/nn5027593.

(33) Schneider, C. A.; Rasband, W. S.; Eliceiri, K. W. NIH Image to ImageJ: 25 Years of Image

Analysis. *Nat. Methods* **2012**, *9* (7), 671–675. https://doi.org/10.1038/nmeth.2089.

(34) Langford, J. I.; Wilson, A. J. C. Scherrer after Sixty Years: A Survey and Some New Results in the Determination of Crystallite Size. *J. Appl. Crystallogr.* **1978**, *11* (2), 102–113. https://doi.org/10.1107/S0021889878012844.

(35) Zhou, Z.; Deng, Y. Kinetics Study of ZnO Nanorod Growth in Solution. *J. Phys. Chem. C* **2009**, *113* (46), 19853–19858. https://doi.org/10.1021/jp907418z.

(36) Bai, S.; Liu, X.; Li, D.; Chen, S.; Luo, R.; Chen, A. Synthesis of ZnO Nanorods and Its Application in NO2 Sensors. *Sensors Actuators, B Chem.* **2011**, *153* (1), 110–116. https://doi.org/10.1016/j.snb.2010.10.010.

(37) Greene, L. E.; Yuhas, B. D.; Law, M.; Zitoun, D.; Yang, P. Solution-Grown Zinc Oxide Nanowires. *Inorg. Chem.* **2006**, *45* (19), 7535–7543. https://doi.org/10.1021/ic0601900.

(38) Strano, V.; Urso, R. G.; Scuderi, M.; Iwu, K. O.; Simone, F.; Ciliberto, E.; Spinella, C.; Mirabella, S. Double Role of HMTA in ZnO Nanorods Grown by Chemical Bath Deposition. *J. Phys. Chem. C* **2014**, *118* (48), 28189–28195. https://doi.org/10.1021/jp507496a.

(39) Sing, K.S.W., Everet, D. H., Haul, R.A.W., Moscou, L., Pierotti, R. A., Rouquerol, J., Siemieniewska, T. Reporting Physisorption Data for Gas/Solid Systems with Special Reference to the Determination of Surface Area and Porosity (Recommendations 1984). *Pure Appl. Chem.* **1985**, *57* (4), 603–619. https://doi.org/10.1351/pac198557040603.

(40) Groen, J. C.; Pérez-Ramírez, J. Critical Appraisal of Mesopore Characterization by Adsorption Analysis. *Appl. Catal. A Gen.* **2004**, *268* (1–2), 121–125.

https://doi.org/10.1016/j.apcata.2004.03.031.

(41)   Viswanadham, N.; Kamble, R.; Singh, M.; Kumar, M.; Murali Dhar, G. Catalytic Properties of Nano-Sized ZSM-5 Aggregates. *Catal. Today* **2009**, *141* (1–2), 182–186. https://doi.org/10.1016/j.cattod.2008.03.026.

(42)   Vachhani, P. S.; Bhatnagar, A. K. Oxygen Pressure-Dependent Band Gap Modification in Cu-Doped and -Undoped ZnO Films. *Phys. Scr.* **2013**, *87* (4). https://doi.org/10.1088/0031-8949/87/04/045702.

(43)   Sagar, P.; Shishodia, P. K.; Mehra, R. M.; Okada, H.; Wakahara, A.; Yoshida, A. Photoluminescence and Absorption in Sol-Gel-Derived ZnO Films. *J. Lumin.* **2007**, *126* (2), 800–806. https://doi.org/10.1016/j.jlumin.2006.12.003.

(44)   Van Dijken, A.; Meulenkamp, E. A.; Vanmaekelbergh, D.; Meijerink, A. Influence of Adsorbed Oxygen on the Emission Properties of Nanocrystalline ZnO Particles. *J. Phys. Chem. B* **2000**, *104* (18), 4355–4360. https://doi.org/10.1021/jp993998x.

(45)   McPeak, K. M.; Le, T. P.; Britton, N. G.; Nickolov, Z. S.; Elabd, Y. A.; Baxter, J. B. Chemical Bath Deposition of ZnO Nanowires at Near-Neutral PH Conditions without Hexamethylenetetramine (HMTA): Understanding the Role of HMTA in ZnO Nanowire Growth. *Langmuir* **2011**, *27* (7), 3672–3677. https://doi.org/10.1021/la105147u.

(46)   Punnoose, A.; Dodge, K.; Rasmussen, J. W.; Chess, J.; Wingett, D.; Anders, C. Cytotoxicity of ZnO Nanoparticles Can Be Tailored by Modifying Their Surface Structure: A Green Chemistry Approach for Safer Nanomaterials. *ACS Sustain. Chem. Eng.* **2014**, *2* (7), 1666–1673. https://doi.org/10.1021/sc500140x.

(47)   Bian, S. W.; Mudunkotuwa, I. A.; Rupasinghe, T.; Grassian, V. H. Aggregation and Dissolution of 4 Nm ZnO Nanoparticles in Aqueous Environments: Influence of PH, Ionic Strength, Size, and Adsorption of Humic Acid. *Langmuir* **2011**, *27* (10), 6059–6068. https://doi.org/10.1021/la200570n.

(48)   Daneshvar, N.; Salari, D.; Khataee, A. R. Photocatalytic Degradation of Azo Dye Acid Red 14 in Water on ZnO as an Alternative Catalyst to TiO2. *J. Photochem. Photobiol. A Chem.* **2004**, *162* (2–3), 317–322. https://doi.org/10.1016/S1010-6030(03)00378-2.

(49)   Lundstedt, T.; Seifert, E.; Abramo, L.; Thelin, B.; Nyström, Å.; Pettersen, J.; Bergman, R. Experimental Design and Optimization. *Chemom. Intell. Lab. Syst.* **1998**, *42* (1–2), 3–40. https://doi.org/10.1016/S0169-7439(98)00065-3.

(50)   Dotto, G. L.; Pinto, L. A. A. Adsorption of Food Dyes onto Chitosan : Optimization Process and Kinetic. *Carbohydr. Polym.* **2011**, *84* (1), 231–238. https://doi.org/10.1016/j.carbpol.2010.11.028.

(51)   Arantes, T. M.; Pinto, A. H.; Leite, E. R.; Longo, E.; Camargo, E. R. Synthesis and Optimization of Colloidal Silica Nanoparticles and Their Functionalization with Methacrylic Acid. *Colloids Surfaces A Physicochem. Eng. Asp.* **2012**, *415*. https://doi.org/10.1016/j.colsurfa.2012.09.041.

(52)   Huang, M.; Weng, S.; Wang, B.; Hu, J.; Fu, X.; Liu, P. Various Facet Tunable ZnO Crystals by a Scalable Solvothermal Synthesis and Their Facet-Dependent Photocatalytic Activities. *J. Phys. Chem. C* **2014**, *118* (44), 25434–25440. https://doi.org/10.1021/jp5072567.

(53)   Li, X.; Wang, J.; Yang, J.; Lang, J.; Cao, J.; Liu, F.; Fan, H.; Gao, M.; Jiang, Y. Size-

Controlled Fabrication of ZnO Micro/Nanorod Arrays and Their Photocatalytic Performance. *Mater. Chem. Phys.* **2013**, *141* (2–3), 929–935. https://doi.org/10.1016/j.matchemphys.2013.06.028.

(54)   Sahnoun, S.; Boutahala, M. Adsorption Removal of Tartrazine by Chitosan/Polyaniline Composite: Kinetics and Equilibrium Studies. *Int. J. Biol. Macromol.* **2018**, *114*, 1345–1353. https://doi.org/10.1016/j.ijbiomac.2018.02.146.

(55)   Rashidi, M.; Sajjadi, S. M.; Mousavi, H. Z. Kinetic Analysis of Azo Dye Decolorization during Their Acid–Base Equilibria: Photocatalytic Degradation of Tartrazine and Sunset Yellow. *React. Kinet. Mech. Catal.* **2019**, *128* (1), 555–570. https://doi.org/10.1007/s11144-019-01654-1.